

Department of Physics and Astronomy
University of Heidelberg

Bachelor thesis

in Physics

submitted by

Kerim Köster

born in Karlsruhe, Germany

August 2018

Nitrogen Vacancy Center Magnetometry as a New Approach for an Active Magnetic Field Control

This Bachelor thesis has been carried out by Kerim Köster

at the

Kirchhoff Institute for Physics

under the supervision of

Prof. Dr. Fred Jendrzejewski

Abstract

This thesis presents the design and implementation of an active magnetic field control setup based on nitrogen vacancy centers in diamond. Magnetic field strengths have been measured using optically detected magnetic resonance techniques. We found that nitrogen vacancy center magnetometry is feasible over a wide range of magnetic field strengths without losing precision. The setup made it possible to measure field strengths with a precision of several ten mG. Implementing a lock-in amplifier enabled the production of an error signal that was fed to a control loop. With this control, magnetic fields were controlled with a bandwidth of 5-10 Hz and a stability of approximately 10 mG. The key parts of the setup that limit the precision and the bandwidth were identified to allow for several improvements that will make it possible to use this approach in ultra cold quantum gas experiments.

Zusammenfassung

Diese Arbeit beschreibt die Entwicklung des Versuchsaufbaus einer aktiven Magnetfeldkontrolle basierend auf Stickstoff-Fehlstellen Zentren in Diamant. Magnetfeldstärken wurden mit der Methode der optisch detektierten Magnetresonanz gemessen. Wir fanden heraus, dass Magnetfeldmessungen mit Stickstoff-Fehlstellen Zentren über einen großen Bereich an Magnetfeldstärken realisierbar sind ohne an Präzision zu verlieren. Diese Methode der Magnetfeldmessung ermöglichte es, Magnetfeldstärken mit einer Präzision von einigen zehn mG zu messen. Durch die Implementierung eines Lock-in Verstärkers in den Versuchsaufbau konnte ein Fehlersignal erzeugt werden, welches zur Magnetfeldkontrolle gebraucht wird. Mit dieser Kontrolle konnten Magnetfeldstärken mit einer Bandbreite von 5-10 Hz und einer Stabilität von etwa 10 mG geregelt werden. Die Bestandteile des Versuchsaufbaus, die die Präzision und die Bandbreite limitierten, konnten identifiziert werden und geben damit eine Grundlage für einige Optimierungen, die es möglich machen, diese Art der Magnetfeldkontrolle für Experimente mit ultrakalten Quantengasen zu nutzen.

Contents

1	Introduction	9
2	Magnetic Field Sensors and Controlling	11
2.1	Magnetic Field Sensors	11
2.2	Magnetic Field Sensing with NV Center Diamonds	13
2.3	Magnetic Field Control	13
3	Nitrogen Vacancy Center Theory	17
3.1	Nitrogen Vacancy Center Basics	17
3.2	Using the Zeeman Shift for Magnetic Field Measurements	20
3.3	Sensitivity	20
4	Magnetometry	23
4.1	Experimental Setup	23
4.2	Preparatory Experiments	25
4.2.1	Calibration	25
4.2.2	Zero-Field Measurement	27
4.3	Magnetic Field Measurement	27
4.3.1	Split Resonances	28
4.3.2	Aligned Diamond Lattice	29
4.4	Lock-In Amplified ODMR Spectra	33
4.4.1	Modified Experimental Setup	33
4.4.2	Lock-In Magnetic Field Measurement	35
5	Active Magnetic Field Control	39
5.1	Closed Loop Configuration	39
5.2	Quality of the Control	41
5.3	Summary and Possible Optimizations	43
5.3.1	Photodiode	45
5.3.2	Laser Intensity	45
5.3.3	Microwave Generator	45
5.3.4	Temperature Control	45
5.3.5	Red Pitaya	46
5.3.6	Measurement Procedure	46
6	Conclusion and Outlook	47

1 Introduction

Complex systems offer a plethora of weird problems. Quantum phenomena of many-particle systems for instance are intriguing in their complexity and are far off from being fully understood. One opportunity to investigate such systems, that can't be solved analytically, is simulating their properties with computers. However, this method hits the wall if one increases the particle number for the considered quantum system due to running out of computational power for many particles.[1]

Richard P. Feynman introduced the idea of *quantum simulators* that can *imitate any quantum system, including the physical world*. [2] Ultracold gases provide a unique platform to be such a quantum simulator that can model quantum many-body physics with control over its microscopic constituents. With this approach one can investigate the mentioned quantum many-body phenomena to which one would not get access with present day computers.

To model a system of interest, control over the quantum simulator's microscopic parameters is essential. One parameter is the interaction between constituents of ultracold quantum gases that can be modified using so-called *Feshbach resonances*. [3] The interaction between atoms close to the Feshbach resonance is magnetic field dependent. The magnetic field where the interaction strength is sensitive to magnetic field fluctuations can be very narrow ($\sim \mu\text{G}$) and also the position of those resonances can be at high magnetic field strengths, ranging up to 1000 G. [4] Also much lower magnetic fields are used for experiments of coherent spin exchange, where the magnetic field is on the same order as the earth's field or even smaller. [5]

Stable magnetic fields with variable strengths over several orders of magnitude are needed and therefore an appropriate sensor and an active control has to be established. One will see that either the working range for commonly used sensors is too low or the sensors are not sensitive for the required stability of the control.

1 Introduction

For that reason, this thesis presents the development of an alternative magnetometer consisting of a nitrogen vacancy (NV) center diamond that has been implemented in a control loop. The manuscript is structured as follows:

Chapter 2 will motivate the decision towards NV centers over commonly used Hall-effect and fluxgate sensors.

Chapter 3 introduces the fundamental theory of NV centers that is required to understand the following chapters and gives information on the theoretically achievable sensitivity.

Chapter 4 presents the experimental setup and the main results of NV magnetometry including the experimental method of optically detected magnetic resonance. The lock-in amplifier is implemented and tested in terms of magnetic field measurement, which lays the foundation for an active magnetic field control.

Chapter 5 describes the implementation of the control loop into the experimental setup of the previous chapter. Experimental results of active stabilization will be presented.

Because the approach to control magnetic fields with NV center magnetometry is totally new, one cannot expect a development of a sensor and control that already meets the above mentioned requirements. It is rather a question of finding out whether this approach hits on fundamental problems that make it impossible to practically use NV center magnetometry and control in ultracold quantum gas experiments. Because no such problems were discovered, the end of this thesis gives several starting points for an optimization of the prototype.

2 Magnetic Field Sensors and Controlling

This chapter motivates the choice of nitrogen vacancy center magnetometry over commonly used sensors. It starts with a discussion of Hall-effect and fluxgate sensors including their limitations as magnetic field sensors in ultracold quantum gas experiments due to the requirements already specified. After that the so-called nitrogen vacancy center is introduced as a promising sensor and its benefits will be discussed. Finally, some basics about controlling will be introduced. This includes properties such as accuracy, stability and bandwidth.

2.1 Magnetic Field Sensors

A magnetic field sensor is the central part of an active magnetic field control. Markets with high demand for magnetometers in areas beyond scientific research include military applications[6], compasses in electronic devices (e.g. mobile phones[7]) and oil/mineral exploration[8]. Depending on their application, specific requirements such as strength and sensitivity differ. However, most types of sensors are constructed to sense magnetic fields in the order of the earth's magnetic field that has a strength of $B_{Earth} \approx 0.5$ G in central Europe. For large field applications, those widely used sensors don't meet our requirements. The sensed fields in ultra cold atom experiments have strengths of several hundred Gauss and should be known with an uncertainty of approximately $10 \mu\text{G}$. There have been two types of sensors, Hall-effect and Fluxgate sensors, that were considered as a potential candidate for the experimental setup before taking into account nitrogen vacancy (NV) centers.

Hall-effect magnetometers use what is referred to as the *Hall Effect*[9] to quantify a magnetic field. This effect creates a voltage in current-carrying (semi)conductors where a static magnetic field has been applied perpendicular to said current. By measuring this so-called Hall voltage U_H one can indirectly measure the magnetic field according to

$$U_H = A_H \frac{IB}{d} \quad (2.1)$$

where I is the current flowing through the (semi)conductor, B is the magnetic field

2 Magnetic Field Sensors and Controlling

strength, d is the thickness of the probe parallel to B and A_H is a material constant. The simplicity of this mechanism makes the whole device easy to handle. There are sensors on the market that can measure field strengths larger than 500 G, which would suffice for the specified requirements. The main disadvantage besides a detailed calibration is its low sensitivity. Good Hall effect sensors reach a sensitivity of 10 mV/G^1 with a noise of more than 10 mV including a bypass capacitance at the power supply inputs. This means that the noise is of the order of 1 G, which is way too high for the specified requirements.

Another method of quantifying a magnetic field is by using fluxgate sensors. This method consists of a magnetically susceptible core wrapped by two coils - one driving coil and one sensing coil. If an alternating voltage is applied to the driving coil, the core produces its own magnetic field that induces a current flowing in the sensing coil. This current averages out over time because both directions are equally likely. If an external magnetic field is applied and the current in the driving coil is high enough to saturate the core's magnetization, one can measure the applied field because one field direction saturates earlier than the other and an asymmetric current signal is produced. The sensitivity of these sensors is very high, especially if a compensation measurement is carried out. Here a third coil is used to compensate the external magnetic field and sets the effective current in the sensing coil to zero again. The compensation current is now directly proportional to the magnetic field. This approach is very complex as one has to control the compensation current and has to set up a program that generates driving pulses with precise duration and repetition frequency. The main disadvantage to using this method, apart from the need for calibration, is the limited magnetic field range where fluxgate sensors work. As they have been developed for working at the earth's magnetic field, they saturate at field strengths of $\sim 10 \text{ G}$.

All in all, three main issues can be summarized that cause problems when sensing magnetic fields:

- Maximum operating range
- Sensitivity
- Complexity (calibration and measurement procedure)

While these three main issues arise when sensing magnetic fields using the two aforementioned methods, the following chapters show that these issues can be avoided when using the nitrogen vacancy (NV) center magnetometer.

¹example datasheet: <https://docs-emea.rs-online.com/webdocs/0d88/0900766b80d88157.pdf>

2.2 Magnetic Field Sensing with NV Center Diamonds

In recent years the NV center has emerged as a promising sensor for magnetic fields and therefore is a real option for the use of an active magnetic field control. Due to their properties as a quantum system they are inherently calibrated, only require fundamental atom and condensed matter physics knowledge, reach sensitivities on the order of μG independent of absolute magnetic field strengths and have a high spatial resolution.

A comparison to the mentioned approaches with Hall-effect and fluxgate sensors can be seen in Table 2.1. The sensing limit, sensitivity and also the size of a potential NV center magnetometer satisfies the requirements better than the others. Now it has to be proved that the NV center approach is realizable and one can implement this magnetometer into a feedback loop to control a magnetic field.

2.3 Magnetic Field Control

An active magnetic field control aims to stabilize a desired field strength against external disturbances like earth's magnetic field fluctuations and electronic noise from laboratory devices. For the stabilization a magnetometer, Helmholtz-coils with a remote-controllable current source for generating homogeneous offset fields and a controlling device are needed (See Figure 2.1). One defines a required setpoint that is continuously compared to the current value delivered by the sensor. Dependent on the deviation that is calculated internally, the Helmholtz coils regulate the field towards the setpoint. An exact description of the controlling device, which is in our case a Proportional Integral (PI) Control, can be gathered from several standard textbooks[12].

The three main requirements for an optimal control are accuracy, stability and a large bandwidth. A control is accurate if the process value and setpoint converge. With a large bandwidth they converge faster, while stability describes the situation where no oscillations around the process value take place and the whole system stays locked even though there are disturbances that cause changes in the magnetic field. These requirements will be checked at the end of this thesis.

Table 2.1: Different Magnetometer Approaches.[11] All numbers are estimations of the order of magnitude.

	Hall-effect	Fluxgate	NV Center
Sensing limit ¹	~1000 G	~10 G	~1000 G
Sensitivity	~1 G	~100 nG	~1 nG[10]
Minimal size ²	~1 mm ³	~10 mm ³	~0.1 mm ³
Complexity ³	Simple functionality Calibration required	Complex functionality Calibration required	Complex functionality Inherently calibrated

¹ maximum measurable field

² sensing volume and size of the used sensor

³ this includes theoretical background, time required for building a setup and the requirement for a calibration

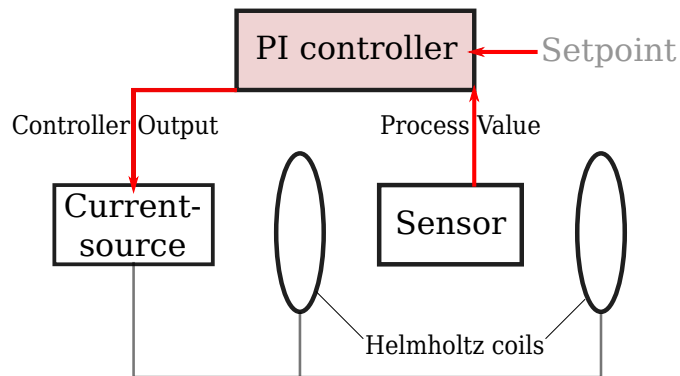


Figure 2.1: Schematic of an active magnetic field control with Helmholtz coils.

The sensor measures the current magnetic field while its output is compared to the setpoint in the controller. Depending on its deviation, it regulates the field strength by a remote control of a pair of Helmholtz coils.

Summary

The use of Hall-effect and fluxgate sensors is not feasible because their working range and sensitivity is not consistent with the specified requirements. NV center magnetometry is a promising candidate for sensing magnetic fields with the required properties because the working range is spread over several orders of magnitude, values of μG resolution can be reached and it is inherently calibrated due to its features as a quantum system. A magnetic field control is characterized by its accuracy, stability and bandwidth. Now, one has to proof that NV center magnetometry can be implemented in a control loop.

3 Nitrogen Vacancy Center Theory

This chapter provides a theoretical background for using NV centers as a quantum sensor. The basic NV center properties, like its solid state nature, level scheme and interaction with optical photons, which leads to excitation and decay processes, will be introduced. The magnetic field dependence comes into play due to the Zeeman effect. The NV center states can be manipulated with microwave photons. For that reason one can get access to its magnetic properties leading to the method of optically detected magnetic resonance. Finally, the magnetic field measurement sensitivity will be introduced theoretically. From this, one can learn about improving the measurement procedure.

3.1 Nitrogen Vacancy Center Basics

The NV center is a point defect in diamond that consists of a nitrogen atom paired with an adjacent vacancy that replace two carbon atoms as depicted in Figure 3.1. The NV center can exist in two charge states, neutral (NV^0) and negatively charged (NV^-). The identifying features of NV^0 and NV^- are their optical zero phonon lines (ZPLs) at 575 nm and 637 nm, respectively. The zero phonon line is the light that is radiated if no phonon participates in the decay process. In the following, NV^0 can be neglected because it does not have detectable magnetic resonances that are required for the following experiments.[16] The ZPL of NV^- is broadened due to photon-phonon interactions¹ at temperatures above absolute zero.[16] This effect can be seen in Figure 3.1. The negatively-charged center has six electrons, two of them unpaired.[17] Two unpaired electrons can form either a singlet state with total spin $S = 0$ or a triplet state with total spin $S = 1$. Nowadays, it is experimentally and theoretically confirmed that both, singlet and triplet state, can exist in an energetic ground and an excited state. The relevant parts of the known level scheme can be seen in Figure 3.2.

¹The phonon coupling generates a continuous emission and absorption spectrum. The phonon sideband is shifted to higher frequency in absorption and to lower frequency in fluorescence due to the Franck-Condon principle.[15]

3 Nitrogen Vacancy Center Theory

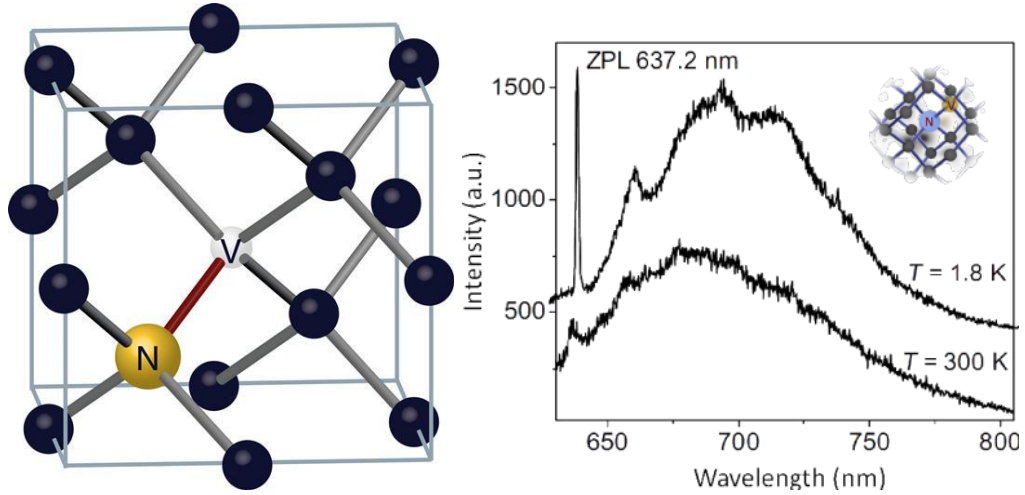


Figure 3.1: Left: Diamond lattice with NV center. The NV center consists of a nitrogen atom (yellow) paired with a vacancy (white) that replace two carbon atoms. *Source:[13]*

Right: Fluorescence spectrum. The zero-phonon-line at 637.2 nm, that is given by the transition from the triplet excited state to the triplet ground state, is broadened due to photon-phonon interactions at temperatures above absolute zero. The peak becomes more indistinct at higher temperatures. This can be seen by comparing the spectra for 1.8 K and 300 K. *Source:[14]*

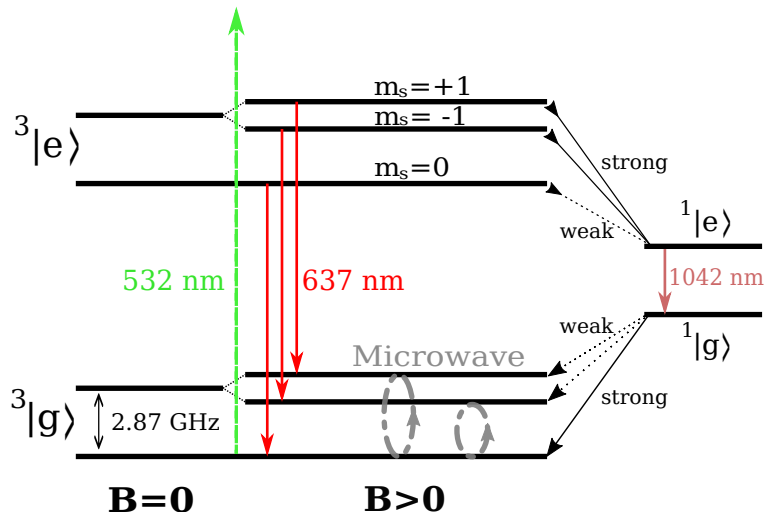


Figure 3.2: Level scheme of NV centers. The characteristic irradiation of a red photon of 637 nm is pumped by a green laser and is described by the transition from the excited triplet to the triplet ground state. The leftmost section shows the energy levels of the triplet states with no magnetic field present, the center section shows the splitting that occurs when a magnetic field is applied and the rightmost section shows the energy levels of the singlet states which will be important for the principle of the optically detected magnetic resonance.

3.1 Nitrogen Vacancy Center Basics

The mentioned ZPL is described by the decay from $^3|e\rangle$ to $^3|g\rangle$ after exciting the electron state optically.² Both, excitation and decay, are in general spin conserving processes. Another decay path is the relaxation through the singlet state which is, in contrast to the fluorescing pathway, a non-radiative (besides of the emission of an infrared photon) and non-spin-conserving decay. Because the probability for the $m_s = \pm 1$ state is higher (compared to the $m_s = 0$ state) to decay via the non-radiative and non-spin-conserving pathway, the system is polarized into the $m_s = 0$ state during optical excitation. A 300 ns excitation leads to a polarization of around 90%.^[19] Since the probability for a non-radiative decay is higher for the $m_s = \pm 1$ excited states, these states emit less fluorescence light, which is a measurable effect. The $m_s = \pm 1$ states emit about 30% less fluorescence.^[20] This will be used for measuring the splitting of the $m_s = 0$ and $m_s = \pm 1$ states.

The structure of the ground state $^3|g\rangle$ with a magnetic field B_z oriented along the NV center axis is modeled by the ground state Hamiltonian^[21], given by

$$H_g = hDm_s^2 + h\gamma B_z m_s \quad (3.1)$$

where h is the Planck constant, D is a zero-field-splitting (ZFS) parameter of approximately 2.87 GHz, $\gamma = g_e\mu_B/h \approx 2.8$ MHz/G³ is the NV gyromagnetic ratio. The zero field splitting is caused by spin-spin interaction between the NV center and the surrounding spins⁴. The whole electron configuration and thus the zero field splitting is dependent on the lattice structure. Larger lattice constants, for instance caused by an increased temperature, lead to less spin-spin interaction which decreases the zero field splitting.^[17] If no magnetic field is applied, the $m_s = \pm 1$ states are degenerate. By applying a magnetic field that has a non-zero component parallel to the NV axis, these two states split apart due to the Zeeman effect. The difference between their shifted energies is

$$\Delta\nu = \frac{\Delta E}{h} = 2\gamma B_z \quad (3.2)$$

where B_z is the projection of the magnetic field to the total spin respectively the projection to a specified NV center axis.

²This excitation is done with a laser of 532 nm wavelength. The electrons are excited to the higher phonon sideband from where they decay to the lowest lying vibrational mode which corresponds to the state that is shown in Figure 3.2. For further information see ^[18].

³ $g_e = 2$: e^- Lande g-factor, $\mu_B = 1.4$ MHz/G: Bohr magneton

⁴For further interest read ^[20]

3.2 Using the Zeeman Shift for Magnetic Field Measurements

The splitting of the $m_s = \pm 1$ states can be used to measure the magnetic field projection along the NV center axes.⁵ This could be done by performing an optically detected magnetic resonance (ODMR) experiment. The triplet ground state is excited continuously by a green laser (typically 532 nm) and therefore becomes polarized in the $m_s = 0$ state. This polarization can now be manipulated by applying a microwave. If its frequency is resonant with the transition of $m_s = 0 \rightarrow m_s = +1$ or $m_s = 0 \rightarrow m_s = -1$ in the ground state, the NV center probe has a higher population of NVs in the $m_s = \pm 1$ state compared to the off-resonant case (see Figure 3.2). This increased population can now be observed as a decreased fluorescence intensity, because those states decay with a higher probability through the non-radiating pathway. By sweeping the microwave frequency and simultaneously recording the fluorescence, one can connect the applied microwave frequency to the resonances that are magnetic field dependent. The field can be calculated using Equation (3.1). By measuring the four magnetic field projections of the respective axis and knowing the unit vectors of the diamond lattice and their orientations relative to the laboratory system one can reconstruct the magnetic field vector. Measuring all four projections is equivalent to determining eight resonance frequencies.

3.3 Sensitivity

The intensity $I(\nu)$ of an ODMR as a function of the applied microwave frequency ν can be approximated by a Lorentz function

$$I(\nu) = R \left[1 - C \left(\frac{\Delta\nu^2}{(\nu - \nu_0)^2 + \Delta\nu^2} \right) \right] \quad (3.3)$$

where R is the photon collection rate, C is the contrast and $\Delta\nu$ is the line width (half-width at half-maximum). Any magnetic field fluctuation δB leads to a shift of the central resonance frequency due to the Zeeman effect. The uncertainty of ν_0 is mainly dependent on the photon shot noise that follows a Poisson distribution. For that reason the intensity's standard deviation δI for a measurement of time duration Δt is $\delta I = \sqrt{I\Delta t}$. The sensitivity η_B is then linked to the minimum detectable magnetic field δB_{\min} by

$$\eta_B(T/\sqrt{Hz}) = \delta B_{\min} \sqrt{\Delta t} \approx \frac{h}{\mu_B g_s} \frac{\sqrt{R}}{\max|\frac{\partial I}{\partial \nu_0}|} = 4/3\sqrt{3} \frac{h}{\mu_B g_s} \frac{\Delta\nu}{C\sqrt{R}}. \quad (3.4)$$

⁵A NV center axis is defined by the tetrahedral structure of the diamond lattice and is always parallel to the vector from an atom to an adjacent atom.

The sensitivity can be minimized by increasing the amount of detected photons R for instance by raising the applied laser power or by increasing the contrast C . This can be achieved by driving the transitions $m_s = 0 \rightarrow m_s = \pm 1$ quicker with increased microwave power. However, both approaches lead to power broadening increasing the linewidth $\Delta\nu$. The optimal sensitivity is a compromise between increasing photon collection R and contrast C whilst paying attention to the power broadening.[22]

Summary

The NV center fluoresces after exciting it optically. One can manipulate the fluorescence intensity by applying a microwave that is resonant to the $m_s = 0 \rightarrow m_s = \pm 1$ transition because those states emit less fluorescence light. The energy difference of these transitions is magnetic field dependent due to the Zeeman effect. These microwave resonance frequencies can be used to extract the projection of the magnetic field to the observed NV center axis. Furthermore, the sensitivity of this measurement depends on the applied laser and microwave power while increasing them leads to a larger sensitivity. In addition one has to be aware of the resonance line's power broadening.

4 Magnetometry

This chapter will explain the experimental setup for the measurement of magnetic fields that are applied by a pair of Helmholtz coils. After calibrating the applied microwave frequency and observing an optically detected magnetic resonance spectrum with zero magnetic field applied, first experimental results on the magnetic field measurement are presented including precision measurements. Afterwards, the setup is extended with a lock-in amplifier that filters out detector noise and produces an error signal. Similar measurements of the field strength and the precision have been carried out.

4.1 Experimental Setup

The setup that uses NV centers as a magnetometer is similar to the one of an ODMR described in [23]. The principle is sketched in Figure 4.1.

A green laser (*Laser Quantum: finesse, 16 W, 532 nm*) is operated at a power of approximately 60 mW. That has been a trade-off between the contrast of the resulting spectrum, power broadening and preventing heat damage. An adjustment of the laser beam in four spatial degrees of freedom was reached by deflecting it with two mirrors before it was focused with a lens of 150 mm focal length onto the diamond to maximize the applied laser power.

The used probe is an ensemble NV center diamond. This means that it has a high concentration of NV centers instead of observing a single defect which leads to an increased photon collection rate. The diamond has a cylindrical shape with (111)-orientation. This means that one of the four diamond axes is orientated perpendicularly to the circular surface. Knowing the orientation is of great interest, because the microwave and the magnetic field have to be adjusted such that resonance shifts and fluorescence reductions (contrast) are maximized. Aligning the circular diamond surface parallel to the area that is encircled by the wire of the Helmholtz coils leads to a maximized magnetic field projection along one NV center axis. In order to optimize the effect of the applied microwave, the antenna adjustment had to be carried out in a way that its generated microwave field is perpendicular to the NV center axis. The microwave frequencies are

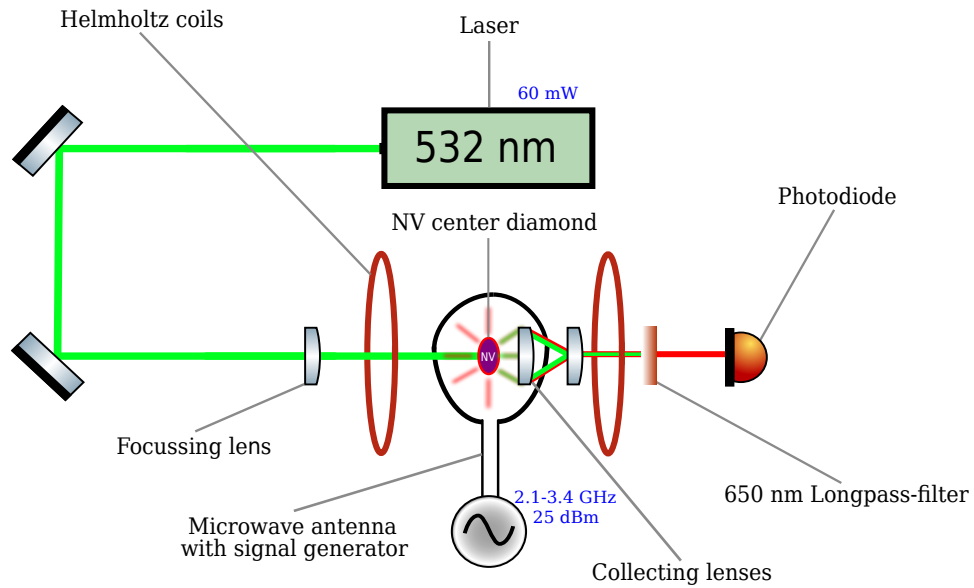


Figure 4.1: Experimental Setup for using the NV center as a magnetometer.

The green laser beam (60 mW) is adjusted by two mirrors and focused by a convex lens onto the diamond sample. The red fluorescence is collected by a parabolic light collecting lens (not displayed) and two lenses with short focal lengths. The green laser light is filtered out with a longpass-filter and the fluorescence is detected using a photodiode. The microwave (25 dBm) is applied onto the NV center diamond by an antenna and a pair of Helmholtz coils is installed to produce a homogeneous magnetic field.

produced by a voltage-controlled oscillator (*Mini-Circuit: ZX95-3360+*), which is tuned by a function generator (*Voltcraft: 8202*). To adjust the applied microwave power, several attenuators and one 30 dB amplifier (*Mini-Circuit: ZVE-3W-83+*) have been installed. Furthermore, a circulator (*Teledyne Microwave: 24022*) has been placed between amplifier and antenna to prevent damage caused by back-reflections. The generated microwave power is approximately 25 dBm, which is enough to drive the transitions.

The fluorescence that can be observed after illuminating the diamond with green laser light is radiated in any spatial direction and thus has to be collected as good as possible because the relative error of each data point is given by the shot noise and thus scales inversely with the square-root of the measured photons. To achieve a maximized photodiode signal, the probe is glued onto a parabolic light collecting lens (*Edmund*

optics: 45°, 2.5 mm Output diameter) that concentrates the whole fluorescence that has been emitted in one half space. In addition to the parabolic lens, two lenses with short focal lengths (*35 mm and 75 mm focal length*) have been installed in order to collect the output light of the diamond-lens setup due to a large emitting angle of 45 degrees of the parabolic lens. A long-pass filter (*Thorlabs: FEL0650*) with a cut-on frequency of 650 nm was brought into the light path in order to filter out the green laser.

The magnetic field that will be measured is produced by a pair of Helmholtz coils. The current is delivered by a high-speed power supply (*Delta Electronica: SM 18-50*).

An ODMR spectrum can now be measured by sweeping the control voltage of the voltage-controlled oscillator (VCO) and thereby the microwave frequency while monitoring the photodiode signal.

4.2 Preparatory Experiments

4.2.1 Calibration

In order to measure magnetic field strengths, the applied microwave frequency has to be well-known. Therefore, the control voltage of the microwave source must be translated into its output frequency. By measuring the control voltage with an oscilloscope and measuring the microwave radiation via a second antenna that was connected to a spectrum analyzer, the calibration was carried out with a quadratic polynomial

$$\nu_{MW}(V) = aV^2 + bV + c \quad (4.1)$$

where ν_{MW} is the microwave frequency, V is the applied control voltage and a, b and c are fit parameters. The result is depicted in Figure 4.2. Errors of measuring the control voltage, such as limiting resolution of the oscilloscope, can now be propagated to errors in frequency domain and thus to an uncertainty of the measured magnetic field. From the error of c one can directly conclude the uncertainty of an absolute frequency as it is of interest when measuring the zero-field splitting of the NV center as mentioned in chapter 3 and measured in 4.2.2.

$$\Delta\nu_{MW} = \Delta c = 10 \text{ MHz} \quad (4.2)$$

For measurements of the magnetic field, this error cancels out by calculating differences of frequencies and thus is not of interest anymore.

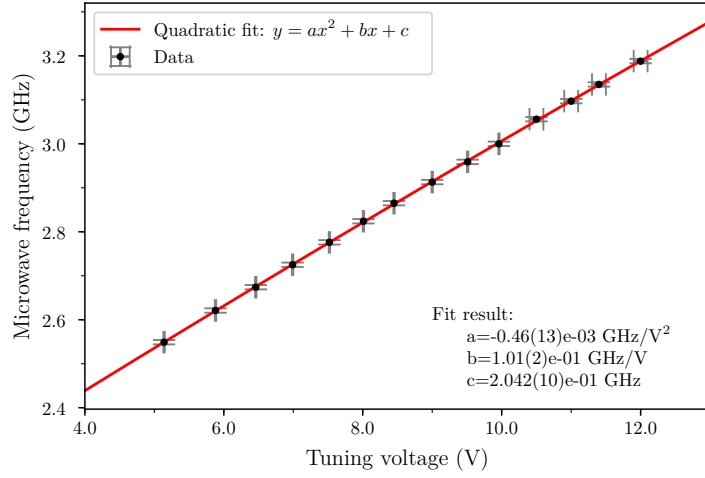


Figure 4.2: Calibration of the microwave frequency. The data has been fitted with a quadratic polynomial to convert the applied control voltage into a microwave frequency. The fit converges well, the pre-factor of the x^3 -term is by a factor 100 smaller than than the pre-factor of the x^2 -term and thus negligible.

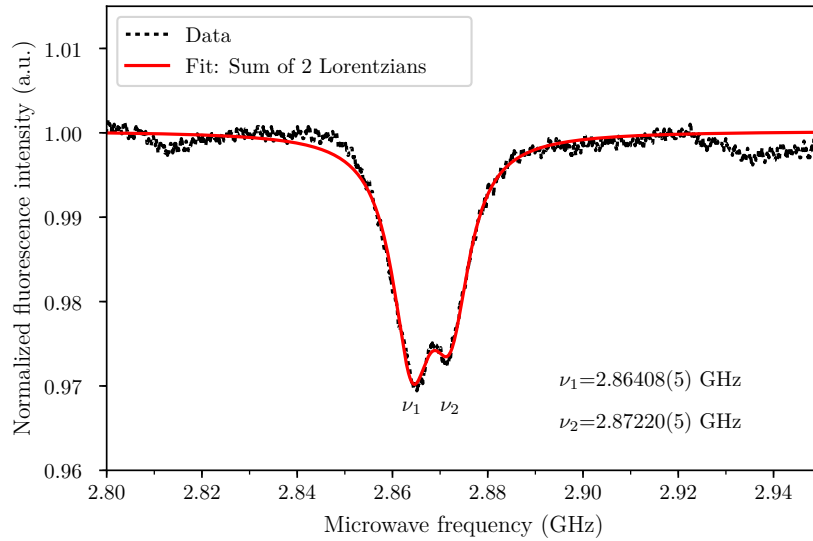


Figure 4.3: Zero field ODMR. The double-dip structure is caused by small external magnetic fields like electronic noise and the earth's magnetic field. A double Lorentz fit has been carried out to extract the resonance frequencies.

4.2.2 Zero-Field Measurement

For measuring the zero field splitting ν_{ZFS} of the $m_s = 0$ and the $m_s = \pm 1$ ground state an ODMR spectrum has been recorded while there is no external magnetic field applied. The signal from Figure 4.3 consists of two superimposed Lorentzian functions. The small splitting is mainly caused by the earth's magnetic field. The fit function for the voltage of the photodiode is:

$$I = \frac{C_1 \Delta \nu_1^2}{(\nu - \nu_1)^2 + \Delta \nu_1^2} + \frac{C_2 \Delta \nu_2^2}{(\nu - \nu_2)^2 + \Delta \nu_2^2} + b \quad (4.3)$$

Here $\Delta \nu_i$ is the half-width at half-maximum (HWHM) of resonance i , $C_i < 0$ is the contrast of dip i , ν_i is the resonance frequency of the respective transition and b is the off-resonant fluorescence level that should be equal to one because the spectra have been normalized. The zero field splitting can now be calculated by simply averaging ν_i . Referring to Part 4.2.1 the error is mainly caused by calibration and hence the result is:

$$\nu_{\text{ZFS}} = 2.868(10) \text{ GHz} \quad (4.4)$$

This is consistent with the expected zero field splitting of 2.87 GHz.[24]

Especially while working with high laser powers $P > 100$ mW, one always has to monitor the temperature of the diamond to avoid damage and this can be done by measuring the zero field splitting. High temperatures above 600 °C lead to an unwanted reorganization of the vacancies[25]. The first order approximation of the temperature dependence around room temperature is:[26]

$$\frac{dT}{d\nu_{\text{ZFS}}} = 12 \text{ K/MHz} \quad (4.5)$$

With this in mind a measured zero field splitting of 2.82 GHz (corresponds to 600 °C) should be alarming.

4.3 Magnetic Field Measurement

Applying a magnetic field to the NV center diamond leads to a splitting of the $m_s = \pm 1$ states. Therefore two minima of fluorescence intensity per axis move symmetrically apart by increasing the field strength. The difference between both dips can now be used to calculate the projection of the applied vector field onto the observed axis.

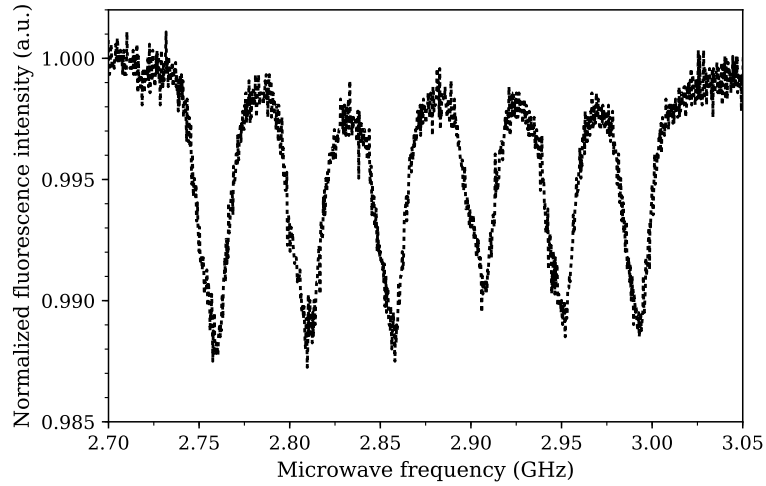


Figure 4.4: ODMR spectrum with split resonances. The spectrum shows six dips. Theoretically it should be possible to observe eight dips because each of the four axes contributes individually with its own resonance frequency to one $m_s = +1$ transition and to one $m_s = -1$ transition. It is possible to reproduce the vector magnetic field from this measurement knowing the orientation of the diamond relative to the laboratory system. However, for some reason two resonances still have the same projection or small differences can not be resolved.

4.3.1 Split Resonances

The ODMR spectrum of a configuration where at least three of the four NV axes experience a different magnetic field projection is depicted in Figure 4.4. One should theoretically be able to observe eight dips if every axis experiences a different magnetic field projection. It could be possible that the linewidth in this experimental setup is too large to resolve small differences of the magnetic field projection and two resonances are simply too close. However, from a spectrum as it is depicted in Figure 4.4, and if the resolution can be increased, it is possible to calculate the vector magnetic field by simple geometry knowing the unit vectors of the diamond structure and the crystal's orientation in the laboratory system. This method is extensively discussed in [23] and is used to map small vector magnetic field structures for instance in microscopy[27]. In this work, the focus is laid on the measurement of a magnetic field that is produced by a pair of Helmholtz coils. Therefore, ideally, one axis is enough to obtain the whole information about the applied magnetic field if the alignment is chosen in a way that has been explained in section 4.1.

4.3.2 Aligned Diamond Lattice

For an aligned axis, which means that one axis is aligned parallel to the magnetic field, the spectrum of Figure 4.4 reduces to only four minimums. The reason is that the other three axes experience the same magnetic field projection and therefore contribute equally to one resonance. In the following measurements the diamond is oriented with maximized projection along the (111)-axis.

Figure 4.5 shows the behavior of ODMR spectra for increasing magnetic fields that have been produced by Helmholtz coils. Additionally, the field strength has been measured with a Gaussmeter with digital output to get a feeling for the visible structures. The resonances move apart more and more with increasing coil current which is synonymous with an increasing magnetic field projection.

As an example measurement, the 20 G spectrum of Figure 4.5 has been chosen to extract the resonance frequencies and therefore calculate the applied field strength, as Figure 4.6 illustrates. Two Lorentz functions have been fitted to the measured data using a simplified version of Equation (4.3):

$$I = \frac{C\Delta\nu^2}{(\nu - \nu_0)^2 + \Delta\nu^2} + b \quad (4.6)$$

From equation (3.1) the magnetic field dependence of the difference $\nu_R - \nu_L$ can be extracted:

$$\nu_R - \nu_L = \delta\nu = 2g_s\mu_B B_{\text{ext}}/h \quad (4.7)$$

Here ν_L and ν_R are the two resonances with $\nu_L < \nu_R$. Calculating differences eliminates the calibration error c and the influence of the temperature-dependent zero field splitting. The magnetic field B_{ext} is then:

$$B_{\text{ext}} = \frac{\delta\nu h}{2g_s\mu_B} \approx \frac{\delta\nu}{2 \cdot 2.8 \frac{\text{MHz}}{\text{G}}} \quad (4.8)$$

The result is then:

$$B_{\text{ext}} = 21.42(2) \text{ G} \quad (4.9)$$

The error has been propagated from the fit error of ν_L and ν_R and is mainly limited to the signal to noise ratio of the measured spectrum and the linewidth of the resonances. The magnetic field that has been measured with the Gaussmeter was: $B_{\text{ext}}^G = 20(1) \text{ G}$. The main error is the sensitivity of the Gaussmeter. This value agrees with the NV center

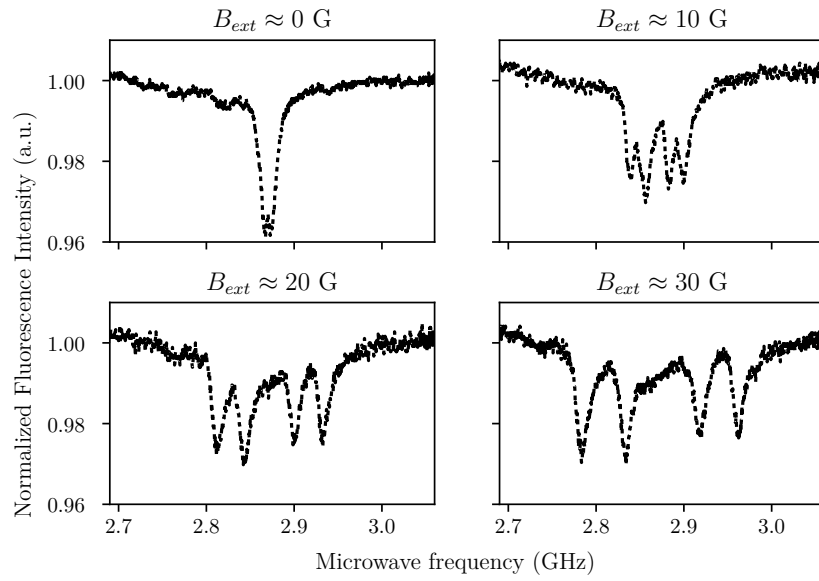


Figure 4.5: ODMR spectrum of four increasing magnetic field strengths applied by Helmholtz coils. The strength has been measured with a digital Gaussmeter. The separation of two corresponding dips is proportional to the magnetic field.

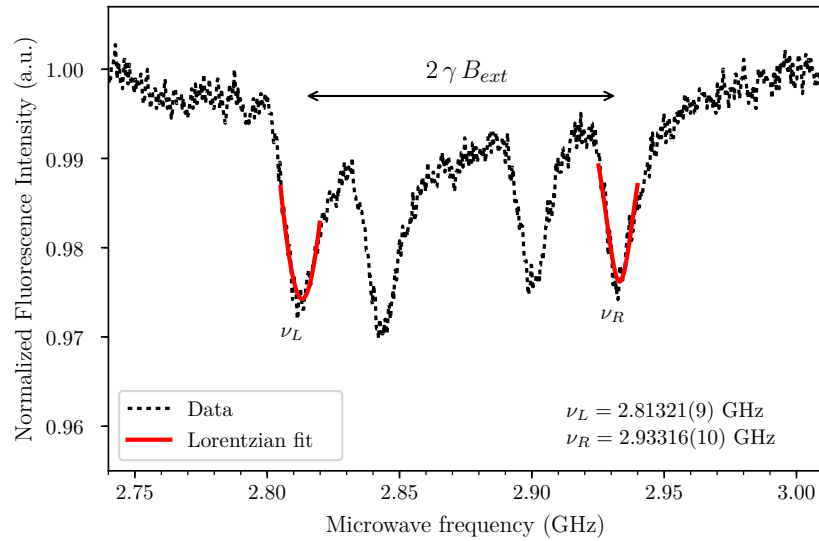


Figure 4.6: ODMR spectrum with an external field of 20 G. The fit has been carried out with a Lorentz function to extract the central resonance frequencies. The separation between two resonances is proportional to the field projection along the specified axis. The width of the two Lorentzians is: $\Delta\nu_L \approx 29$ MHz and $\Delta\nu_R \approx 8$ MHz.

measurement within their error margins.¹

One main theoretical advantage when using NV center magnetometers is the independence of linewidth and magnetic field strength that leads to a mainly constant absolute error of the magnetic field. This aspect makes it possible to use NV centers for measuring high fields with high sensitivity. An ODMR spectrum for a 20 A coil current has been recorded to prove this and is shown in Figure 4.7. According to Equation (4.8) the magnetic field is:

$$B_{\text{ext}} = 68.25(3) \text{ G} \quad (4.10)$$

Compared to the result of Equation (4.9) one can see that the fit error increased by ~ 10 mG. On the other hand the HWHM parameter $\Delta\nu$ effectively decreased because the dips are set wider apart and therefore the Lorentz function looks sharper. The reason for a higher magnetic field error is a decrease of data points that have been taken into account for the fit because the sweep range is larger. However, the HWHM parameters prove that the line width of the resonances does not increase by raising the magnetic field strength which is an important feature for high magnetic field measurements.

In the previous calculations, statistical fluctuations have not been taken into account. To make statements on this uncertainty, about 30 measurements with identical coil current ($I = 5.00$ A) and with an integration time of $\tau_{\text{int}} = 1$ s have been carried out. This has been achieved by averaging 128 times directly on the oscilloscope with a sweep frequency of $f_{\text{sweep}} = 128$ Hz. After calculating the magnetic field for each measurement with (4.8), one can compute the standard deviation of measuring magnetic fields with an unchanged coil current. The results are summarized in a histogram (see Figure 4.8). The measured precision is:

$$\Delta B_{\text{ext}}(\tau_{\text{int}}) = 37 \text{ mG} \quad (4.11)$$

This value is integration time dependent because noise with a frequency f in principal averages out after a time $\tau_{\text{int}} \gtrsim 1/f$. To describe this dependency, one can record a whole precision spectrum. For this it would be useful to have an automated measurement procedure that takes the data for varying integration times because it would have been very unhandy to measure each spectrum on its own.

An extended method for measuring magnetic field strengths has been performed with the use of a lock-in amplifier, which reduces noise and also will be mandatory for the magnetic field control because it modifies the spectrum's shape.

¹The deviation D between both measurements is: $D = (1.4 \pm 1.0) \text{ G}$. This corresponds to a 1.4σ deviation, which is not significant.

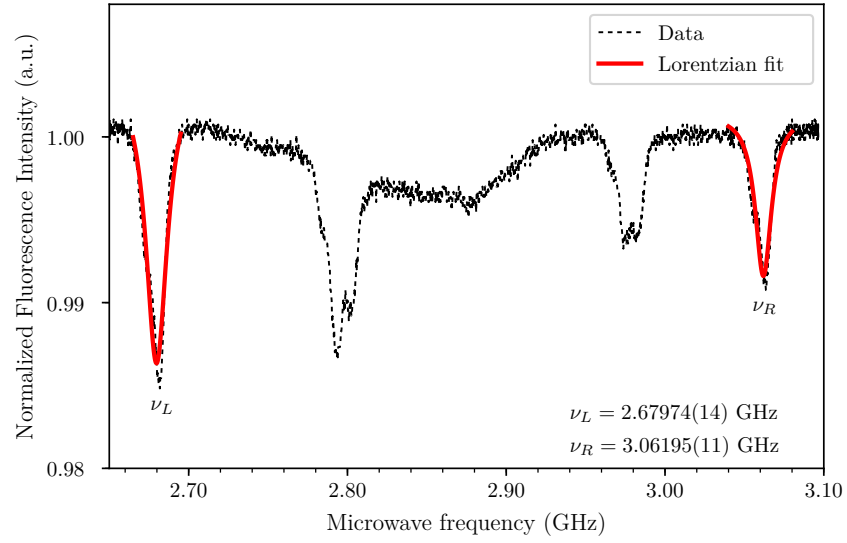


Figure 4.7: ODMR spectrum of a magnetic field produced by a coil current of 20 A. The resonances have been fitted with a Lorentz function. The HWHM parameters $\Delta\nu_{L/R}$ are: $\Delta\nu_L \approx 8$ MHz and $\Delta\nu_R \approx 6$ MHz. The splitting of the inner dips is caused by a small misalignment of the other three NV center axes relative to the applied magnetic field.

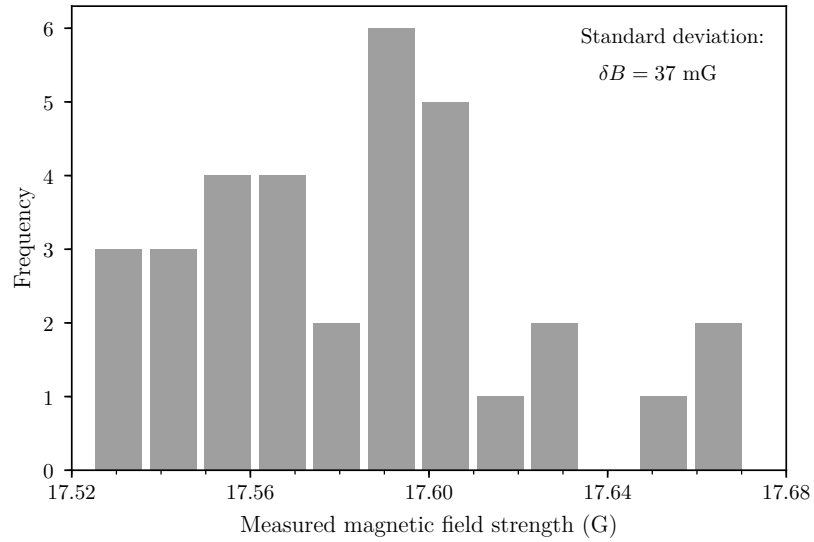


Figure 4.8: Histogram of measured magnetic field strengths with constant coil current. For each measurement the integration time was $\tau_{\text{int}} = 1$ s.

4.4 Lock-In Amplified ODMR Spectra

4.4.1 Modified Experimental Setup

The difference between the experimental setup of Figure 4.9 in comparison to the one in Figure 4.1 is the use of a lock-in amplifier (*Stanford Research: SR830*) to increase the signal to noise ratio by eliminating detector noise. The lock-in amplifier provides a modulation frequency of 6 kHz with an amplitude of 8 mV (reference oscillator) which corresponds to approximately 1 MHz modulation depth. This is connected to a summing amplifier that produces a signal corresponding to the sum of the modulation signal and the triangular sweep signal. The summed signal is connected to the control voltage input of the VCO that delivers the microwave frequency. The summing amplifier was built according to the scheme in Figure 4.10. The photodiode signal is now also modulated with 6 kHz if the original ODMR spectrum has a slope unequal to zero at the measured data point. The fluorescence signal goes to the input of the lock-in amplifier where the signal is demodulated. This means that the fluorescence signal is mixed with the modulation signal and thus produces sum and difference frequency components. The output of the mixer is then low-pass filtered with a selectable cut-off frequency f_c that is connected to the specified adjustable time constant TC^2 via

$$TC = \frac{1}{2\pi f_c}. \quad (4.12)$$

Now, frequency components close to the modulation frequency will be mixed down to DC and pass through the low-pass filter. The result is that noise with a frequency not close to 6 kHz will not pass the combination of mixer and low-pass filter. One can interpret the lock-in amplifier as a bandpass filter with an adjustable narrow passband.

Another effect of using a lock-in amplifier is reshaping the spectrum such that it is proportional to the derivative of the initial ODMR spectrum (see Figure 4.6). This statement can be motivated by looking at two cases. Modulating the microwave frequency at a point where the absolute gradient is unequal to zero produces an AC signal that produces a measurable lock-in signal. A larger absolute gradient will also increase the amplitude of the AC signal and thus the lock-in voltage. At the center of a magnetic resonance the slope of the spectrum is equal to zero. Here a modulation of the microwave frequency does not result in an AC signal. Therefore, no signal can pass through the

²In the following measurements the time constant was chosen such that the error signal does not contain visible noise anymore but is still as low as possible because high time constants slow down the data recording and will also slow down a magnetic field control. The chosen time constant was: $TC = 100 \mu s$.

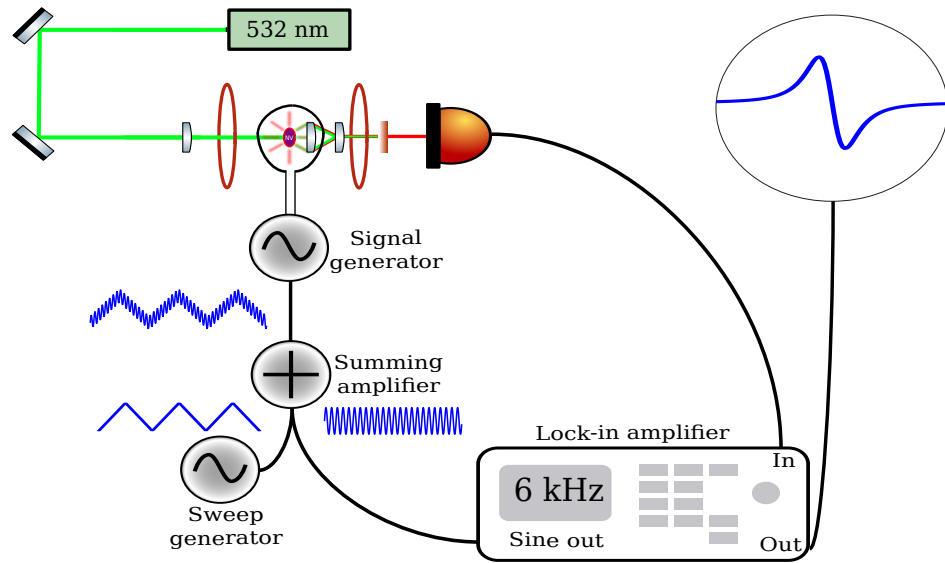


Figure 4.9: Modified setup for recording an error signal. A lock-in amplifier has been installed that outputs a 6 kHz sine signal to a summing amplifier where it is modulated by a triangular function from a function generator like in Section 4.1. The result is a frequency-modulated triangular function that results in a frequency-modulated microwave frequency. This modulation could now be observed on the photodiode too, which is fed back to the lock-in amplifier that produces the error signal.

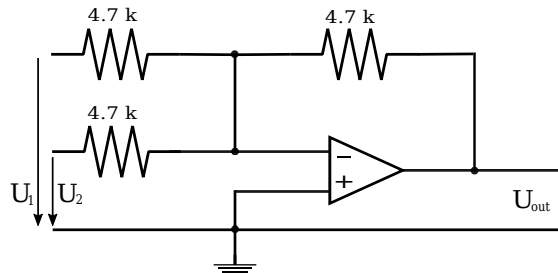


Figure 4.10: Summing amplifier. This electronic circuit is used to sum the modulation signal and the triangular sweep voltage. The two inputs and the output are connected to the inverting input of an operational amplifier via one 4.7 k Ω resistor respectively. The ground is connected to the non-inverting input. U_{out} can now be used to record a microwave sweep with a frequency-modulated control voltage.

combination of mixer and lowpass filter. One can conclude that the lock-in amplifier provides a signal that is proportional to the gradient of the ODMR spectrum where inflection points provide large lock-in voltages and extrema become zero-crossings. The fact that resonances become zero-crossings is an extremely useful feature for control loops as it will be made clear in Chapter 5.

4.4.2 Lock-In Magnetic Field Measurement

The measurement procedure is the same as in Section 4.3 except for the fit function. As mentioned in Subsection 4.4.1, the lock-in signal is proportional to the derivative of the photodiode signal which has the shape of a Lorentz function. Differentiating Equation (4.6) leads to:

$$E = \frac{dI}{d\nu} = \frac{-2C\Delta\nu^2(\nu - \nu_0)}{((\nu - \nu_0^2) + \Delta\nu^2)^2}. \quad (4.13)$$

The resonance frequencies ν_{0i} can be extracted from the fit and are shown in Figure 4.11. From this and Equation (4.8) one can calculate the magnetic field which is:

$$B_{\text{ext}} = 17.86(2) \text{ G} \quad (4.14)$$

The error is the same as in Equation (4.9). Therefore, the lock-in approach does not lead to a more precise magnetic field measurement. This statement can be confirmed by looking at Figure 4.12. Here the standard deviation has been measured by recording around 30 measurements with a current of $I = 5.00 \text{ A}$. The integration time was $\tau_{\text{int}} = 1 \text{ s}$. This has been achieved by averaging over 16 measurements with a sweep frequency of 16 Hz. It became clear that higher sweep frequencies do not work because the low-pass filter of the lock-in amplifier suppresses higher frequencies specified by the chosen time constant. One can see that the standard deviation of measurements with and without a lock-in amplifier do not differ significantly. So, for measuring the magnetic field strength, a lock-in amplifier is not useful in the described setup. But as discussed in [23] and [28] it is very practical for carrying out real-time measurements of the resonance frequencies because you do not have to record a whole spectrum but you can focus on single resonances using a feedback loop. This will be discussed more extensively in the following Chapter.

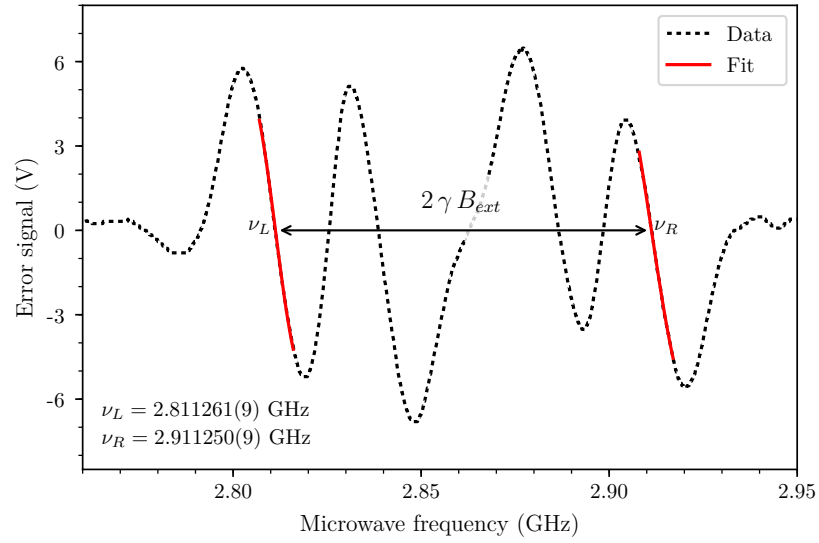


Figure 4.11: ODMR spectrum provided by a lock-in amplifier. The data has been fitted using Equation 4.13 to extract the resonance frequencies. The magnetic field projection onto the NV axis can now be calculated with the illustrated difference of resonance frequencies.

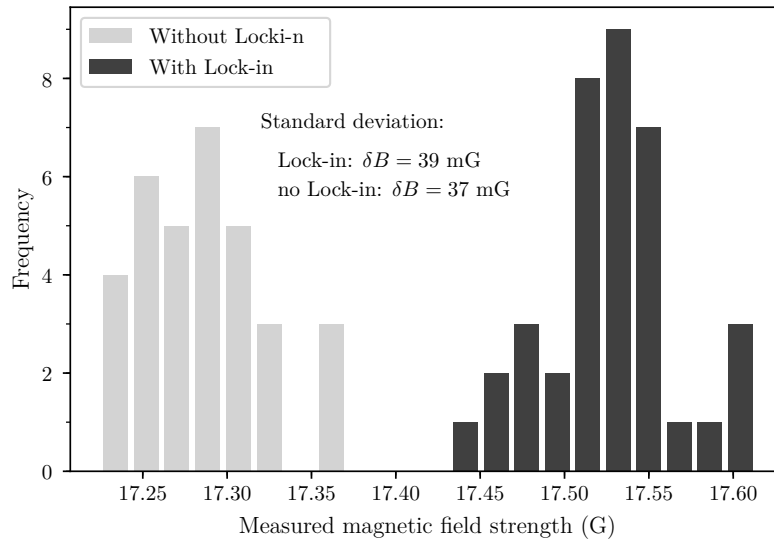


Figure 4.12: Measurement noise at 1 s integration time with and without a lock-in amplifier. The precisions with and without the lock-in amplifier (standard deviations) do not deviate significantly. The difference of the mean between the two approaches is due to slightly different current source settings.

Summary

Several conclusions can be drawn from this chapter:

- The measurement of the zero-field-splitting can be used to determine the temperature of the probe. High temperatures should be prevented to avoid damage.
- The magnetic field strength can be measured with an absolute precision of approximately 40 mG independent of the chosen setup (with and without a lock-in amplifier).
- The strength of an applied magnetic field does not influence the absolute uncertainty because the linewidth is independent of the field strength.
- The lock-in setup provides an error signal that is required for the magnetic field control.
- Averaging was unavoidable because the photodiode signal was extremely noisy. This slows down the data acquisition. For the same reason one is forced to increase the time constant of the lock-in amplifier to achieve a smooth error signal. The disadvantage is that this aspect limits the bandwidth of a magnetic field control.

5 Active Magnetic Field Control

In this chapter the lock-in setup (Figure 4.9) is implemented in a closed loop to control the magnetic field that is produced by a pair of Helmholtz-coils. Therefore, the hardware and software for the control loop is described and the main idea behind this specific control approach is explained in detail. Afterwards the quality of the control is analyzed to make statements about accuracy, stability and bandwidth. As already mentioned, the results give rise to several optimization options that are stated at the end of this chapter.

5.1 Closed Loop Configuration

To operate the setup of Figure 4.9 in closed loop, which means that the error signal is used to control the magnetic field in the center of the Helmholtz-coil configuration, a PI-controller is needed. The hardware, that was used, is a *Red Pitaya* with a 10 Bit analog-to-digital- and digital-to-analog-converter. *Red Pitaya* is an open-source hardware project that can replace several laboratory instruments such as an oscilloscope, a spectrum analyzer and a signal generator. To operate the Red Pitaya hardware as a PI-controller an additional software package *PyRPL*¹ has been used. It is an open-source software package that provides tools such as the just mentioned PI-controller or also a lock-in amplifier or several filters with graphical user interfaces.

The main idea in locking the magnetic field strength was to set the microwave frequency to a value that corresponds to the resonance frequency of the required magnetic field strength. One can calculate this frequency from the ground-state Hamiltonian (3.1) with

$$\nu_{\text{MW}\pm}(B_{\text{ext}}) = 2.87 \text{ GHz} \pm 2.8 \frac{\text{MHz}}{\text{G}} \cdot B_{\text{ext}}. \quad (5.1)$$

It does not matter whether one chooses the higher or lower microwave frequency because of the symmetry of the Zeeman effect. The following measurements have been carried out with $\nu_{\text{MW}-}$ that corresponds to the $m_s = 0 \rightarrow m_s = -1$ transition. Now the control is responsible for ensuring that the resonance stays at the set microwave frequency. This is

¹The functionality of this open-source software package is documented at: <http://pyrpl.readthedocs.io/en/latest/gui.html>

5 Active Magnetic Field Control

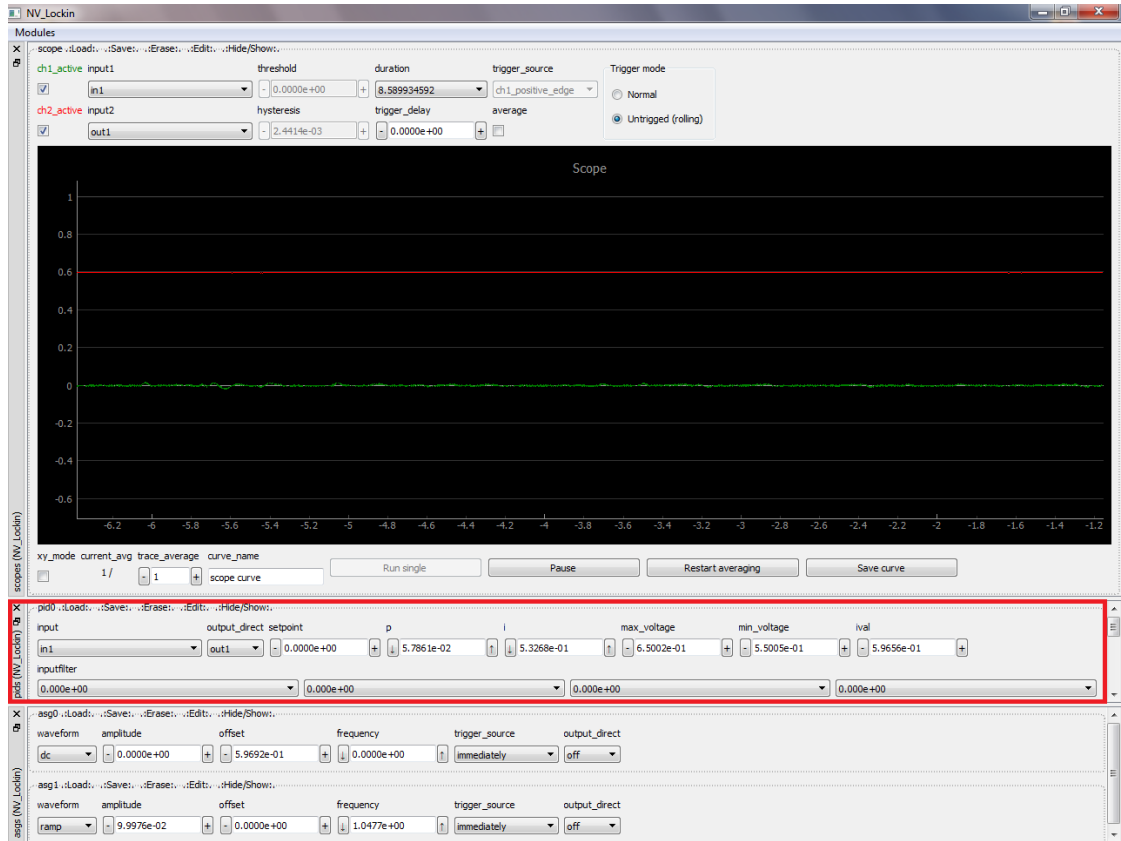


Figure 5.1: PyRPL PI widget. *input* is the error signal, *output* is the control voltage of the current source. The *setpoint* is set to zero to focus on the central frequency of the resonance. By adjusting *p* and *i* one can lock the error signal to zero. *max_voltage* and *min_voltage* have to be chosen such that the control voltage of the Helmholtz-coils is in the capturing range. Once the magnetic field is locked, the range can be enlarged. *ival* is a value that integrates the deviation of setpoint and current value, *inputfilter* can be chosen to highpass or lowpass filter the input error signal. The other two tools that are provided by PyRPL that have been used are *scopes* (oscilloscope) and *asgs* (function generator).

equivalent to a constant magnetic field strength, neglecting temperature dependent drifts of the zero field splitting. Therefore, the zero-crossing of the error signal (compare 4.11) that corresponds to the specified resonance is controlled to be at a constant microwave frequency by adjusting the current of the Helmholtz-coils. The controller, as introduced in Figure 2.1, has two connections to the experimental setup - one input connection (process value), which is the error signal delivered by the lock-in amplifier, and one output connection (controller output), which is the remote control of the coils current source. The PI-control tool of *PyRPL* (see the graphical user interface of Figure 5.1) works with those two connections as specified in *input* and *output_direct*. The setpoint is set to zero to focus on the resonance. To make sure that one detects the resonance and not the off-resonant area where the error signal is zero too, one has to set *max_voltage* and *min_voltage* in a way such that the resonance is in the capturing range. This is the range between two adjacent local extrema of the error signal's zero crossing. Otherwise the magnetic field cannot be locked, because the controller would regulate towards an off-resonant value of the error signal that is also zero. This capturing range can easily be measured by sweeping the control voltage of the current source and reading off the position of the local adjacent extrema of the resonance. Proportional gain p and integral gain i have been adjusted until the system was locked to zero. The lock is successful if the system follows a change of the setpoint.

5.2 Quality of the Control

The quality of the control can be estimated by looking at the locked and unlocked error signal and calculating the standard deviation. The recorded time trace is depicted in Figure 5.2 for both cases. The standard deviation of the microwave frequency of the resonance can then be calculated with the slope of a corresponding ODMR spectrum and can be converted to an uncertainty of the magnetic field strength using the gyromagnetic ratio γ . The results can be seen in Table 5.1. One can summarize that, at the moment, the controlled magnetic field standard deviation is not remarkably smaller than the uncontrolled magnetic field standard deviation. However, the frequency of the noise spectrum shifted towards higher frequencies which means that the control suppresses noise up to 5-10 Hz. Low frequency drifts can be suppressed by the control. Therefore also DC magnetic field deviations from the desired magnetic field strength can be avoided.

Another approach to assess the quality of the control is to check the response of the system to a change of the setpoint for instance by applying a step function that modulates the frequency of the microwave. A change of the microwave frequency forces

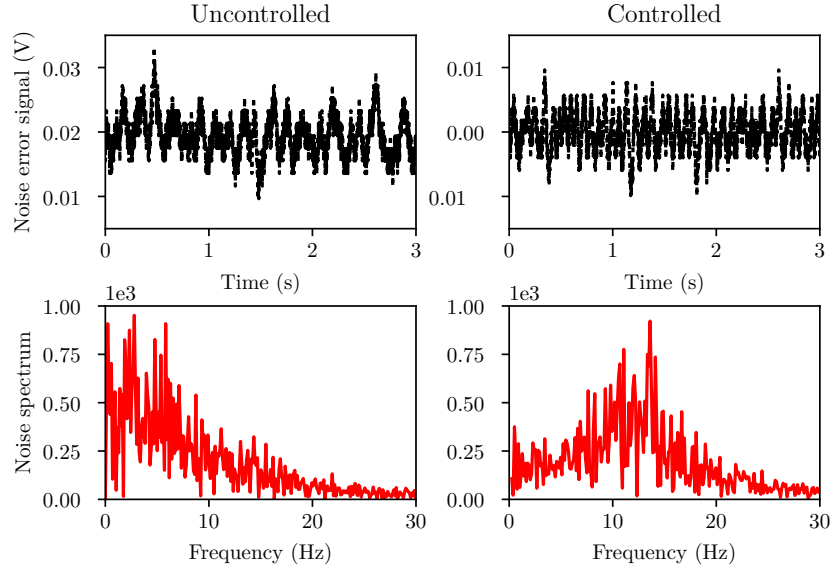


Figure 5.2: Time trace and spectrum of controlled and uncontrolled error signal. The two graphs on the top show the time trace of the error signal. The standard deviation is very similar but different frequency components contribute. The bottom graphs show the Fourier transform of the time trace. The control reduces noise up to approximately 5 Hz and increases noise between 5 Hz and 15 Hz due to instabilities in this frequency region.

Table 5.1: Accuracy of controlled and uncontrolled magnetic field

	STD error signal (mV)*	STD magnetic field (mG)**
Controlled	3.09	9.4
Uncontrolled	3.39	10.3

* STD of the time trace of Figure 5.2

** conversion of the STD of the error signal based on the slope of the zero-crossing of a corresponding ODMR spectrum and the gyromagnetic ratio γ

the control to change the magnetic field until the zero-crossing is at the position of the applied microwave frequency. The setpoint of the PI-control is still at zero but the applied microwave frequency is changed. To apply this modulation, the summing amplifier from Figure 4.10 is extended with a third input voltage. Now, one input delivers a DC offset voltage that specifies the central frequency of the microwave, one input adds the modulation of the lock-in amplifier (6 kHz) and one input adds a low frequency step function to implement a stepwise change of the magnetic field strength. The result can be seen in Figure 5.3. One can read off the settling time of the control by estimating the width of the error signal dips. The width² is approximately 0.1 to 0.2 seconds. This matches with the bandwidth of the control of approximately 5 Hz that can be estimated from the noise spectrum of Figure 5.2. One can increase the rise time of the step function response by increasing the integral gain (see Figure 5.4) but that also leads to a larger overshoot and unwanted oscillations. The maximum amplitude of the modulation and thus the maximum change of the magnetic field, where the control is still locked, is limited by the capturing range that is mainly the linewidth of the resonances.

5.3 Summary and Possible Optimizations

This chapter showed that a control over the applied magnetic field is possible. Low-frequency noise has been reduced and the magnetic field, measured at the NV center axes, can be modified for instance with a step function inside the capturing range of the locked resonance. However, there have been several notable problems that occurred with the magnetic field measurement and magnetic field control:

- Long data acquisition time because of low signal to noise ratio. The result is a small bandwidth of the control and an amplification of 5 Hz - 15 Hz noise.
- No automated measurement procedure and therefore no possibility to do long time measurements or to acquire a large amount of data.
- The calibration of the microwave leads to a non-accurate microwave frequency.
- The temperature-dependence of the zero field splitting can lead to a misinterpreted frequency shift which becomes important when measuring only absolute frequencies as it is done in the magnetic field control.
- Only minor improvement of the magnetic field stability in closed-loop configuration

²The width is estimated as the difference of two zero-crossings.

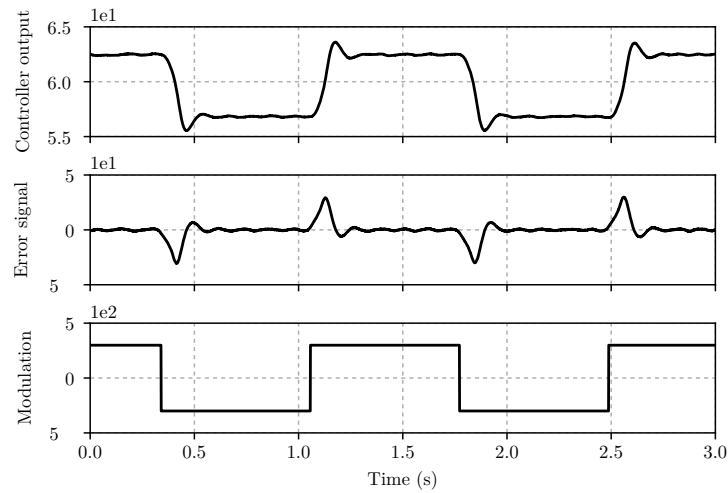


Figure 5.3: Step function response of the magnetic field control. The bottom picture shows the modulation that was added to an offset voltage to change the microwave frequency. Here, a modulation larger than zero leads to a decrease of the microwave frequency due to an inverting summing amplifier. A decrease of the microwave frequency corresponds to a larger magnetic field strength, because the control is locked to the $m_s = 0 \rightarrow m_s = -1$ transition. The response of the magnetic field is visualized indirectly as a response of the controller output that influences the coil current. The error signal indicates the deviation of setpoint and current value. From that one can estimate the settling time which is 0.1-0.2 s. Settling time and the observable overshoot depend on integral gain and proportional gain.

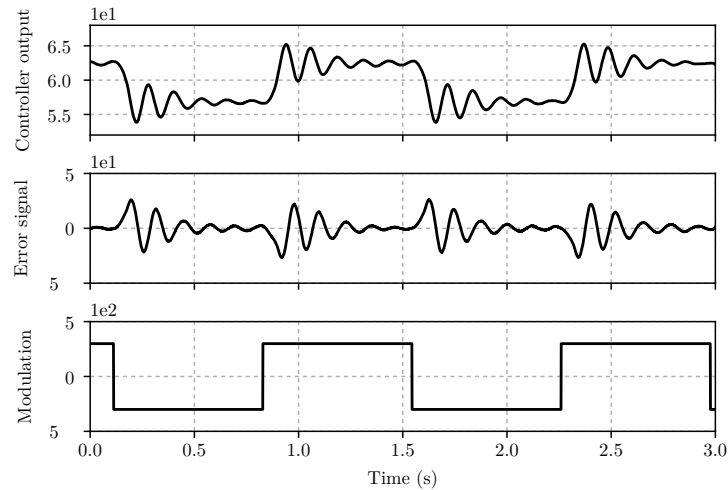


Figure 5.4: Step function response for an increased integral gain. The increased integral gain leads to larger oscillations, so that the control is about to become unstable.

5.3.1 Photodiode

Probably the most sensitive part of the experimental setup is the photodiode. Without averaging over the output of the photodiode amplifier, the signal to noise ratio is approximately 2:1 (20 mV contrast and 10 mV noise). This is the main reason, why the time constant of the lock-in amplifier cannot be set to smaller values, increasing the data acquisition time. This way, it decreases the bandwidth and the stability of the control a lot. Noise sources mainly are laser intensity fluctuations, electric noise of surrounding parts of the setup (microwave, power supply) and internal photodiode noise. In order to optimize this part of the setup, one has to install a photodiode that can reduce the mentioned noise sources. This can be reached with a so-called balanced photodiode that consists of two photodiodes - one for detecting the fluorescence and one reference photodiode that measures the laser intensity. The noise that is detected by the reference photodiode is then internally subtracted from the measurement photodiode, which would reduce the influence of external electronic noise and laser noise significantly.

5.3.2 Laser Intensity

The laser is operated at less than one percent of its maximum output power. This leads to very unstable laser intensities that result in noise of the detected fluorescence. This also contributes to long data acquisition times and long time constants of the lock-in amplifier. As a first step, one could increase the output power of the laser to make it work more stable and focus only a small fraction of the whole power onto the diamond with a halfwave-plate and a polarizing beam splitter. A more laborious approach would be to implement an active intensity control with an acousto-optic modulator (AOM).[29] One has to test whether this is still required with the use of the balanced photodiode.

5.3.3 Microwave Generator

The microwave frequency is adjusted by a control voltage that is applied to the voltage-controlled oscillator. To decrease the uncertainty of the applied frequency one can use a professional microwave signal generator where the frequency can be set digitally and the microwave power can be adjusted to optimize the contrast.

5.3.4 Temperature Control

As already mentioned in Section 3.1, the zero field splitting is temperature dependent. This leads to a shift of absolute resonance frequencies. This effect is negligible if only

5 Active Magnetic Field Control

the difference between two dips is used to measure the magnetic field strength. However, in closed-loop mode only the absolute frequency is used, because only one microwave frequency can be applied to lock the zero-crossing to a specified value. Here, an increase of the temperature, for instance due to laser irradiation, has the same effect as an increase of the magnetic field strength (for the $m_s = 0 \rightarrow m_s = -1$ transition). A constant temperature that can be achieved by cooling or by an active temperature control would solve this issue.

5.3.5 Red Pitaya

At the moment, the 10 Bit resolution of the Red Pitaya is no limiting feature for the magnetic field control due to more influential issues, as discussed above. However, at some point the digitalization that leads to a discretization of 2 mV sensitivity can be problematic. A hardware update to the 14 Bit version of Red Pitaya will increase the sensitivity by a factor of 16.

5.3.6 Measurement Procedure

Most of the measurements have been carried out by adjusting all parameters by hand and recording the data using an oscilloscope. This makes it hard to improve the measurement procedure just by changing parameters that include sweep frequency, laser power, microwave power, lock-in modulation depth/frequency, time constant and much more. For an optimized use of the magnetic field control, at some point, one has to automate and digitize the measurement parameters and data acquisition.

6 Conclusion and Outlook

This thesis reports on the design and implementation of an active magnetic field control with a nitrogen-vacancy center magnetometer. The experimental setup combines optics and electronics as well as atomic and condensed matter physics.

Magnetic fields have been measured with an uncertainty of approximately 40 mG at one second integration time by recording ODMR spectra. Here, the absolute magnetic field strength does not influence the uncertainty, which means that also large fields can be measured with equal absolute uncertainty. The magnetic field error did not decrease after implementing a lock-in amplifier, but it was necessary for producing an error signal which was fed to a PI-controller. The final magnetic field control has a bandwidth of approximately 5-10 Hz and makes it possible to suppress low frequency drifts of the magnetic field. Within the capturing range and bandwidth one can modulate the magnetic field produced by Helmholtz coils for instance with a step function.

The next steps will include optimizations of the central parts of the setup. To increase the bandwidth and the accuracy of the control, a balanced photodiode will be implemented and the laser intensity has to be stabilized. The final goal is to put the the diamond on top of the end of an optical fiber, surrounded by a microwave antenna. The green laser is guided through the fiber and the fluorescence, that is emitted into the fiber, is collected. In this case, the whole electronics can be located at a distance such that the sensor is compact and can be brought as near as possible to the volume where the magnetic field has to be stabilized.¹

An interesting approach to prevent the coupling of temperature drifts and magnetic field locking is described in [28]. Here, the microwave frequency can be locked to more than one resonance at the same time by applying different microwave frequencies simultaneously and reading out each locked resonance frequency. Then it would be possible to measure differences of the resonance frequencies which are temperature independent and also measurements in real-time of more than one resonance can be done, for instance to reproduce the vector magnetic field without recording a whole spectrum.

¹This method was introduced by the group of Jörg Wrachtrup.[30]

Bibliography

- [1] K. Brown, W. Munro, and V. Kendon, “Using quantum computers for quantum simulation,” *ENTROPY*, vol. 12, no. 11, pp. 2268–2307, 2010.
- [2] R. P. Feynman, “Simulating physics with computers,” *International Journal of Theoretical Physics*, vol. 21, no. 6-7, pp. 467–488, 1982.
- [3] C. Chin, R. Grimm, P. Julienne, and E. Tiesinga, “Feshbach resonances in ultracold gases,” *REVIEWS OF MODERN PHYSICS*, vol. 82, no. 2, pp. 1225–1286, 2010.
- [4] A. Trautmann, *Spin dynamics and Feshbach resonances in ultracold Sodium-Lithium mixtures*. 2016.
- [5] D. Stamper-Kurn and M. Ueda, “Spinor bose gases: Symmetries, magnetism, and quantum dynamics,” *REVIEWS OF MODERN PHYSICS*, vol. 85, no. 3, pp. 1191–1244, 2013.
- [6] P. Ripka, “Review of fluxgate sensors,” *Sensors & Actuators: A. Physical*, vol. 33, no. 3, pp. 129–141, 1992.
- [7] A. Allan, *Basic sensors in iOS*. Sebastopol, CA: O’Reilly, 1st ed ed., 2011.
- [8] J. P. Morin, K. A. Kurrus, P. Leung, S. Fan, and D. Symmonds, *Applications and anomalies in NDBC’s oil and gas platform ADCP ocean current data*. Marine Technology Society, 2017.
- [9] E. H. Hall, “On a new action of the magnet on electric currents,” *American Journal of Mathematics*, vol. 2, no. 3, pp. 287–292, 1879.
- [10] T. Wolf, P. Neumann, K. Nakamura, H. Sumiya, T. Ohshima, J. Isoya, and J. Wrachtrup, “Subpicotesla diamond magnetometry,” *PHYSICAL REVIEW X*, vol. 5, no. 4, p. 041001, 2015.
- [11] J. Lenz and S. Edelstein, “Magnetic sensors and their applications,” *IEEE Sensors Journal*, vol. 6, no. 3, pp. 631–649, 2006.

Bibliography

- [12] S. W. Sung, J. Lee, and I.-B. Lee, *Process identification and PID control*. Singapore: Wiley, 2009.
- [13] K. Beha, H. Fedder, M. Wolfer, M. C. Becker, P. Siyushev, M. Jamali, A. Batalov, C. Hinz, J. Hees, L. Kirste, H. Obloh, E. Gheeraert, B. Naydenov, I. Jakobi, F. Dolde, S. Pezzagna, D. Twittchen, M. Markham, D. Dregely, H. Giessen, J. Meijer, F. Jelezko, C. E. Nebel, R. Bratschitsch, A. Leitenstorfer, and J. Wrachtrup, “Diamond nanophotonics,” *Beilstein journal of nanotechnology*, vol. 3, no. 1, pp. 895–908, 2012.
- [14] P. Allen, “Putting a new spin on things.” <https://www.chemistryworld.com/news/putting-a-new-spin-on-things/3007939.article>, 2017. [Online; accessed 07-August-2018].
- [15] J. Friedrich and D. Haarer, “Photochemical hole burning: A spectroscopic study of relaxation processes in polymers and glasses,” *Angewandte Chemie International Edition in English*, vol. 23, no. 2, pp. 113–140, 1984.
- [16] M. W. Doherty, N. B. Manson, P. Delaney, F. Jelezko, J. Wrachtrup, and L. C. Hollenberg, “The nitrogen-vacancy colour centre in diamond,” *Physics Reports*, vol. 528, no. 1, pp. 1–45, 2013.
- [17] M. W. Doherty, N. B. Manson, P. Delaney, and L. C. L. Hollenberg, “The negatively charged nitrogen-vacancy centre in diamond: the electronic solution,” *New Journal of Physics*, vol. 13, no. 2, p. 025019, 2011.
- [18] Y. Rosenzweig, “The physics of nitrogen-vacancy color centers in diamonds and their interaction with external fields,” 2016.
- [19] L. Robledo, H. Bernien, T. v. d. Sar, and R. Hanson, “Spin dynamics in the optical cycle of single nitrogen-vacancy centres in diamond,” *New Journal of Physics*, vol. 13, no. 2, p. 025013, 2011.
- [20] V. Ivady, T. Simon, J. R. Maze, I. A. Abrikosov, and A. Gali, “Pressure and temperature dependence of the zero-field splitting in the ground state of nv centers in diamond: A first-principles study,” *Physical Review B*, vol. 90, no. 23, p. 235205, 2014.
- [21] S. Li, L. Yang, D. Cao, Y. Wang, F. Shuang, and F. Gao, “Identifying different mechanisms in the control of a nitrogen vacancy center system,” *Physics Letters A*, vol. 381, no. 38, pp. 3276–3281, 2017.

- [22] A. Dreau, M. Lesik, L. Rondin, P. Spinicelli, O. Arcizet, J.-F. Roch, and V. Jacques, “Avoiding power broadening in optically detected magnetic resonance of single nv defects for enhanced dc magnetic field sensitivity,” *Physical Review B*, vol. 84, no. 19, 2011.
- [23] C. Teale, “Magnetometry with ensembles of nitrogen vacancy centers in bulk diamond,” 2015.
- [24] J. Wang, F. Feng, J. Zhang, J. Chen, Z. Zheng, L. Guo, W. Zhang, X. Song, G. Guo, L. Fan, C. Zou, L. Lou, W. Zhu, and G. Wang, “High-sensitivity temperature sensing using an implanted single nitrogen-vacancy center array in diamond,” *Physical Review B*, vol. 91, no. 15, 2015.
- [25] P. Deak, B. Aradi, M. Kaviani, T. Frauenheim, and A. Gali, “Formation of nv centers in diamond: A theoretical study based on calculated transitions and migration of nitrogen and vacancy related defects,” *Physical Review B*, vol. 89, no. 7, 2014.
- [26] G.-C. Guo, Z.-F. Han, J.-M. Cui, F.-W. Sun, X.-D. Chen, C.-L. Zou, and C.-H. Dong, “Temperature dependent energy level shifts of nitrogen-vacancy centers in diamond,” *Applied Physics Letters*, vol. 99, no. 16, pp. 161903–161903–3, 2011.
- [27] B. Maertz, A. I. Wijnheijmer, G. Fuchs, M. Nowakowski, and D. Awschalom, “Vector magnetic field microscopy using nitrogen vacancy centers in diamond,” *Applied Physics Letters*, vol. 96, no. 9, p. 092504, 2010.
- [28] H. Clevenson, L. Pham, C. Teale, K. Johnson, D. Englund, and D. Braje, “Robust high-dynamic-range vector magnetometry with nitrogen-vacancy centers in diamond,” *APPLIED PHYSICS LETTERS*, vol. 112, no. 25, p. 252406, 2018.
- [29] C. Giehr, “Laser intensity stabilisation,” 2014.
- [30] S. Hirschmann, “Diamond - a flawless sensor.” <https://www.pi3.uni-stuttgart.de/news/Diamond-a-flawless-sensor/>, 2018. [Online; accessed 07-August-2018].

List of Figures

2.1	Schematic of an active magnetic field control with Helmholtz coils. The sensor measures the current magnetic field while its output is compared to the setpoint in the controller. Depending on its deviation, it regulates the field strength by a remote control of a pair of Helmholtz coils.	14
3.1	Left: Diamond lattice with NV center. The NV center consists of a nitrogen atom (yellow) paired with a vacancy (white) that replace two carbon atoms. <i>Source:[13]</i> Right: Fluorescence spectrum. The zero-phonon-line at 637.2 nm, that is given by the transition from the triplet excited state to the triplet ground state, is broadened due to photon-phonon interactions at temperatures above absolute zero. The peak becomes more indistinct at higher temperatures. This can be seen by comparing the spectra for 1.8 K and 300 K. <i>Source:[14]</i>	18
3.2	Level scheme of NV centers. The characteristic irradiation of a red photon of 637 nm is pumped by a green laser and is described by the transition from the excited triplet to the triplet ground state. The leftmost section shows the energy levels of the triplet states with no magnetic field present, the center section shows the splitting that occurs when a magnetic field is applied and the rightmost section shows the energy levels of the singlet states which will be important for the principle of the optically detected magnetic resonance.	18
4.1	Experimental Setup for using the NV center as a magnetometer. The green laser beam (60 mW) is adjusted by two mirrors and focused by a convex lens onto the diamond sample. The red fluorescence is collected by a parabolic light collecting lens (not displayed) and two lenses with short focal lengths. The green laser light is filtered out with a longpass-filter and the fluorescence is detected using a photodiode. The microwave (25 dBm) is applied onto the NV center diamond by an antenna and a pair of Helmholtz coils is installed to produce a homogeneous magnetic field.	24

4.2 **Calibration of the microwave frequency.** The data has been fitted with a quadratic polynomial to convert the applied control voltage into a microwave frequency. The fit converges well, the pre-factor of the x^3 -term is by a factor 100 smaller than than the pre-factor of the x^2 -term and thus negligible. 26

4.3 **Zero field ODMR.** The double-dip structure is caused by small external magnetic fields like electronic noise and the earth’s magnetic field. A double Lorentz fit has been carried out to extract the resonance frequencies. 26

4.4 **ODMR spectrum with split resonances.** The spectrum shows six dips. Theoretically it should be possible to observe eight dips because each of the four axes contributes individually with its own resonance frequency to one $m_s = +1$ transition and to one $m_s = -1$ transition. It is possible to reproduce the vector magnetic field from this measurement knowing the orientation of the diamond relative to the laboratory system. However, for some reason two resonances still have the same projection or small differences can not be resolved. 28

4.5 **ODMR spectrum of four increasing magnetic field strengths applied by Helmholtz coils.** The strength has been measured with a digital Gaussmeter. The separation of two corresponding dips is proportional to the magnetic field. 30

4.6 **ODMR spectrum with an external field of 20 G.** The fit has been carried out with a Lorentz function to extract the central resonance frequencies. The separation between two resonances is proportional to the field projection along the specified axis. The width of the two Lorentzians is: $\Delta\nu_L \approx 29$ MHz and $\Delta\nu_R \approx 8$ MHz. 30

4.7 **ODMR spectrum of a magnetic field produced by a coil current of 20 A.** The resonances have been fitted with a Lorentz function. The HWHM parameters $\Delta\nu_{L/R}$ are: $\Delta\nu_L \approx 8$ MHz and $\Delta\nu_R \approx 6$ MHz. The splitting of the inner dips is caused by a small misalignment of the other three NV center axes relative to the applied magnetic field. 32

4.8 **Histogram of measured magnetic field strengths with constant coil current.** For each measurement the integration time was $\tau_{\text{int}} = 1$ s. . 32

4.9 **Modified setup for recording an error signal.** A lock-in amplifier has been installed that outputs a 6 kHz sine signal to a summing amplifier where it is modulated by a triangular function from a function generator like in Section 4.1. The result is a frequency-modulated triangular function that results in a frequency-modulated microwave frequency. This modulation could now be observed on the photodiode too, which is fed back to the lock-in amplifier that produces the error signal. 34

4.10 **Summing amplifier.** This electronic circuit is used to sum the modulation signal and the triangular sweep voltage. The two inputs and the output are connected to the inverting input of an operational amplifier via one 4.7 kΩ resistor respectively. The ground is connected to the non-inverting input. U_{out} can now be used to record a microwave sweep with a frequency-modulated control voltage. 34

4.11 **ODMR spectrum provided by a lock-in amplifier.** The data has been fitted using Equation 4.13 to extract the resonance frequencies. The magnetic field projection onto the NV axis can now be calculated with the illustrated difference of resonance frequencies. 36

4.12 **Measurement noise at 1 s integration time with and without a lock-in amplifier.** The precisions with and without the lock-in amplifier (standard deviations) do not deviate significantly. The difference of the mean between the two approaches is due to slightly different current source settings. 36

5.1 **PyRPL PI widget.** *input* is the error signal, *output* is the control voltage of the current source. The *setpoint* is set to zero to focus on the central frequency of the resonance. By adjusting *p* and *i* one can lock the error signal to zero. *max_voltage* and *min_voltage* have to be chosen such that the control voltage of the Helmholtz-coils is in the capturing range. Once the magnetic field is locked, the range can be enlarged. *ival* is a value that integrates the deviation of setpoint and current value, *inputfilter* can be chosen to highpass or lowpass filter the input error signal. The other two tools that are provided by PyRPL that have been used are *scopes* (oscilloscope) and *asgs* (function generator). 40

5.2 **Time trace and spectrum of controlled and uncontrolled error signal.** The two graphs on the top show the time trace of the error signal. The standard deviation is very similar but different frequency components contribute. The bottom graphs show the Fourier transform of the time trace. The control reduces noise up to approximately 5 Hz and increases noise between 5 Hz and 15 Hz due to instabilities in this frequency region. 42

5.3 **Step function response of the magnetic field control.** The bottom picture shows the modulation that was added to an offset voltage to change the microwave frequency. Here, a modulation larger than zero leads to a decrease of the microwave frequency due to an inverting summing amplifier. A decrease of the microwave frequency corresponds to a larger magnetic field strength, because the control is locked to the $m_s = 0 \rightarrow m_s = -1$ transition. The response of the magnetic field is visualized indirectly as a response of the controller output that influences the coil current. The error signal indicates the deviation of setpoint and current value. From that one can estimate the settling time which is 0.1-0.2 s. Settling time and the observable overshoot depend on integral gain and proportional gain. 44

5.4 **Step function response for an increased integral gain.** The increased integral gain leads to larger oscillations, so that the control is about to become unstable. 44

Danksagung

Für die letzten fünf Monate während meiner Bachelorarbeit möchte ich mich bei folgenden Personen bedanken:

- Danke Fred, für dieses super coole Thema und dein Vertrauen, mich nach Stuttgart zu schicken und eine hoffentlich ergiebige Kooperation zu starten. Deine Begeisterung für die Physik und deine lockere Art mit deinen Studenten umzugehen ist sehr beeindruckend. Ich werde mich gerne an die Zeit in deiner Gruppe erinnern.
- Danke Thomas, für deine Bereitschaft als Zweitprüfer meine Arbeit zu korrigieren und meinem Bachelorkolloquium am MPIK einen Rahmen zu bieten. Dein offenkundiges Interesse an meinem Thema hat mich sehr gefreut.
- Danke an die Stuttgarter Gruppe von Jörg Wrachtrup für euer Vertrauen mir einen eurer Diamanten auszuleihen. Ein besonderer Dank geht dabei auch an Julia und Jakob für eure fachliche Unterstützung bei meiner Arbeit.
- Danke an das ganze NaLi/SoPa-Team mit: Apoorva, Lilo, Rohid, Jan, kleiner Alex, Fabián, großer Alex und Kai. Es war immer schön, euch in Labor oder Büro anzutreffen. Ein besonderer Dank geht an Jan und kleiner Alex fürs Korrekturlesen und an Kai und großer Alex für die experimentelle Unterstützung meiner Arbeit.
- Danke an die gesamte Matterwave/SynQs Gemeinschaft, die mir beim gemeinsamen Frühstück den Freitag versüßt hat, stets interessiert an meiner Arbeit war und mir bei jeder Frage oder Materialknappheit ausgeholfen hat. Ein besonderer Dank geht an Helmut, ohne den ich wahrscheinlich immer noch auf die Hälfte der Bauteile meines Versuchsaufbaus warten würde und um einige physikalische Erkenntnisse ärmer wäre.
- Und natürlich auch danke an meine Familie und meine Freunde, die mich außerhalb der Universität unterstützt haben und für den nötigen Ausgleich gesorgt haben. In diesem Sinne auch danke Marc und Megan für den sprachlichen Feinschliff.

Erklärung

Ich versichere, dass ich diese Arbeit selbstständig verfasst habe und keine anderen als die angegebenen Quellen und Hilfsmittel benutzt habe.

Heidelberg, den 21.08.2018

.....